

# Ultrahigh-Resolution Imaging of the Human Brain with Phase-Cycled Balanced Steady-State Free Precession at 7 T

Michael M. Zeineh, MD, PhD, Mansi B. Parekh, PhD, Greg Zaharchuk, PhD, MD, Jason H. Su, MS, Jarrett Rosenberg, PhD, Nancy J. Fischbein, MD, and Brian K. Rutt, PhD

**Objectives:** The objectives of this study were to acquire ultra-high resolution images of the brain using balanced steady-state free precession (bSSFP) at 7 T and to identify the potential utility of this sequence.

**Materials and Methods:** Eight volunteers participated in this study after providing informed consent. Each volunteer was scanned with 8 phase cycles of bSSFP at 0.4-mm isotropic resolution using 0.5 number of excitations and 2-dimensional parallel acceleration of  $1.75 \times 1.75$ . Each phase cycle required 5 minutes of scanning, with pauses between the phase cycles allowing short periods of rest. The individual phase cycles were aligned and then averaged. The same volunteers underwent scanning using 3-dimensional (3D) multiecho gradient recalled echo at 0.8-mm isotropic resolution, 3D Cube T2 at 0.7-mm isotropic resolution, and thin-section coronal oblique T2-weighted fast spin echo at  $0.22 \times 0.22 \times 2.0$ -mm resolution for comparison. Two neuroradiologists assessed image quality and potential research and clinical utility.

**Results:** The volunteers generally tolerated the scan sessions well, and composite high-resolution bSSFP images were produced for each volunteer. Rater analysis demonstrated that bSSFP had a superior 3D visualization of the micro-architecture of the hippocampus, very good contrast to delineate the borders of the subthalamic nucleus, and relatively good B1 homogeneity throughout. In addition to an excellent visualization of the cerebellum, subtle details of the brain and skull base anatomy were also easier to identify on the bSSFP images, including the line of Gennari, membrane of Lilliequist, and cranial nerves. Balanced steady-state free precession had a strong iron contrast similar to or better than the comparison sequences. However, cortical gray-white contrast was significantly better with Cube T2 and T2-weighted fast spin echo.

**Conclusions:** Balanced steady-state free precession can facilitate ultrahigh-resolution imaging of the brain. Although total imaging times are long, the individually short phase cycles can be acquired separately, improving examination tolerability. These images may be beneficial for studies of the hippocampus, iron-containing structures such as the subthalamic nucleus and line of Gennari, and the basal cisterns and their contents.

**Key Words:** bSSFP, FIESTA, hippocampus, subthalamic nucleus, high resolution, 7 T, SRLM, brain

(*Invest Radiol* 2014;49: 278–289)

Ultrahigh-field magnetic resonance imaging offers the promise of improved visualization of anatomy and micropathology in the human central nervous system.<sup>1,2</sup> Despite the challenges posed by high-field physics, many groups have developed or optimized techniques to

produce stunning images of the brain. Two-dimensional T2\*-weighted sequences were the first to be widely used, taking advantage of natural iron-based contrast at high field.<sup>3–8</sup> Susceptibility mapping takes advantage of this iron contrast in phase imaging to produce impressive images of the deep gray nuclei at 7 T.<sup>9</sup> Variations on spoiled gradient-recalled echo have been used for T1-weighted imaging with resolution as high as 0.5-mm isotropic,<sup>10</sup> and specialized image acquisition and processing can mitigate the B1 transmit and receive inhomogeneities.<sup>11</sup> Fluid-attenuated inversion recovery requires magnetization preparation and delivers high contrast applicable to disorders such as multiple sclerosis.<sup>12</sup> T2-weighted fast spin echo (FSE) has been used to depict the details of the human hippocampal formation.<sup>13</sup> Each of these techniques has benefits and limitations at 7 T. Most are subject to marked signal intensity heterogeneity attributable to wavelength effects.<sup>14–17</sup> More importantly, there is a need for whole-brain and/or skull-base sequences with clinically useful contrast at a resolution significantly beyond what can be performed at 3.0 T (ie, smaller than 0.6-mm isotropic with T2 weighting).

Balanced steady state-free precession (bSSFP) is a sequence in routine clinical use for detecting pathology involving the cranial nerves and skull base because of its excellent cerebrospinal fluid (CSF)–tissue contrast.<sup>18</sup> Furthermore, bSSFP demonstrates iron sensitivity<sup>19</sup> and is an efficient sequence with a high intrinsic signal-to-noise ratio (SNR).<sup>20</sup> At 7 T, phase imaging with bSSFP has demonstrated SNR benefits compared with gradient recalled echo (GRE) per unit imaging time.<sup>21</sup> Although bSSFP suffers from bands of signal hypointensity due to B0 inhomogeneity, these can be remedied by phase cycling.<sup>22,23</sup> Finally, bSSFP can be performed with low flip angles to avoid the limitations on the specific absorption rate (SAR) that can often be prohibitive at 7 T. Because bSSFP is relatively unexplored at ultrahigh field, we sought to acquire very high-resolution bSSFP images of the whole brain at 7 T and to compare them with more standard imaging sequences. We specifically hypothesized that bSSFP, because of its intrinsically high SNR and near-microscopic resolution achievable at 7 T, will be superior to other commonly used 7 T techniques in the visualization of the small intricate structures such as the hippocampal formation, iron-containing nuclei such as the subthalamic nucleus, and the cranial nerves within the basilar cisterns.

## MATERIALS AND METHODS

### Acquisition

Six young, healthy controls and 2 patients with epilepsy provided informed consent in accordance with the Stanford institutional review board and Health Insurance Portability and Accountability Act. They were scanned with a 7 T GE Discovery MR950 scanner using a Nova radiofrequency coil (quadrature transmit, 32-channel receive). After acquiring localizers and performing high-order B0 shimming to approximately 20 Hz root mean square uniformity, we acquired 8 increments of phase-cycled bSSFP (3-dimensional [3D] fast imaging employing steady-state acquisition [FIESTA], coronal, frequency superior-inferior repetition time [TR] of 8.2 milliseconds, echo time [TE] of 4.1 milliseconds, field angle of 25 degrees, number of excitations (NEX) of 0.5 with 32 overscans [extra lines beyond the center of k-space], bandwidth [BW] of 62 kHz, field of view [FOV] of 17 cm,  $420 \times 420$

Received for publication July 24, 2013; and accepted for publication, after revision, October 11, 2013.

From the Department of Radiology, Stanford University, Stanford, CA.

Conflicts of interest and sources of funding: Dr Zeineh has received funding from GE Healthcare. Dr Rutt has received funding from GE Healthcare and the National Institutes of Health (P41 EB015891-19). For the other authors listed, no conflicts are declared.

Supplemental digital contents are available for this article. Direct URL citations appear in the printed text and are provided in the HTML and PDF versions of this article on the journal's Web site ([www.investigativeradiology.com](http://www.investigativeradiology.com))

Reprints: Michael Zeineh, MD, PhD, Department of Radiology, Stanford University, Lucas Center for Imaging, Room P271, 1201 Welch Rd, 94305-5488 Stanford, CA. E-mail: [mzeineh@stanford.edu](mailto:mzeineh@stanford.edu).

Copyright © 2014 by Lippincott Williams & Wilkins

ISSN: 0020-9996/14/4905-0278

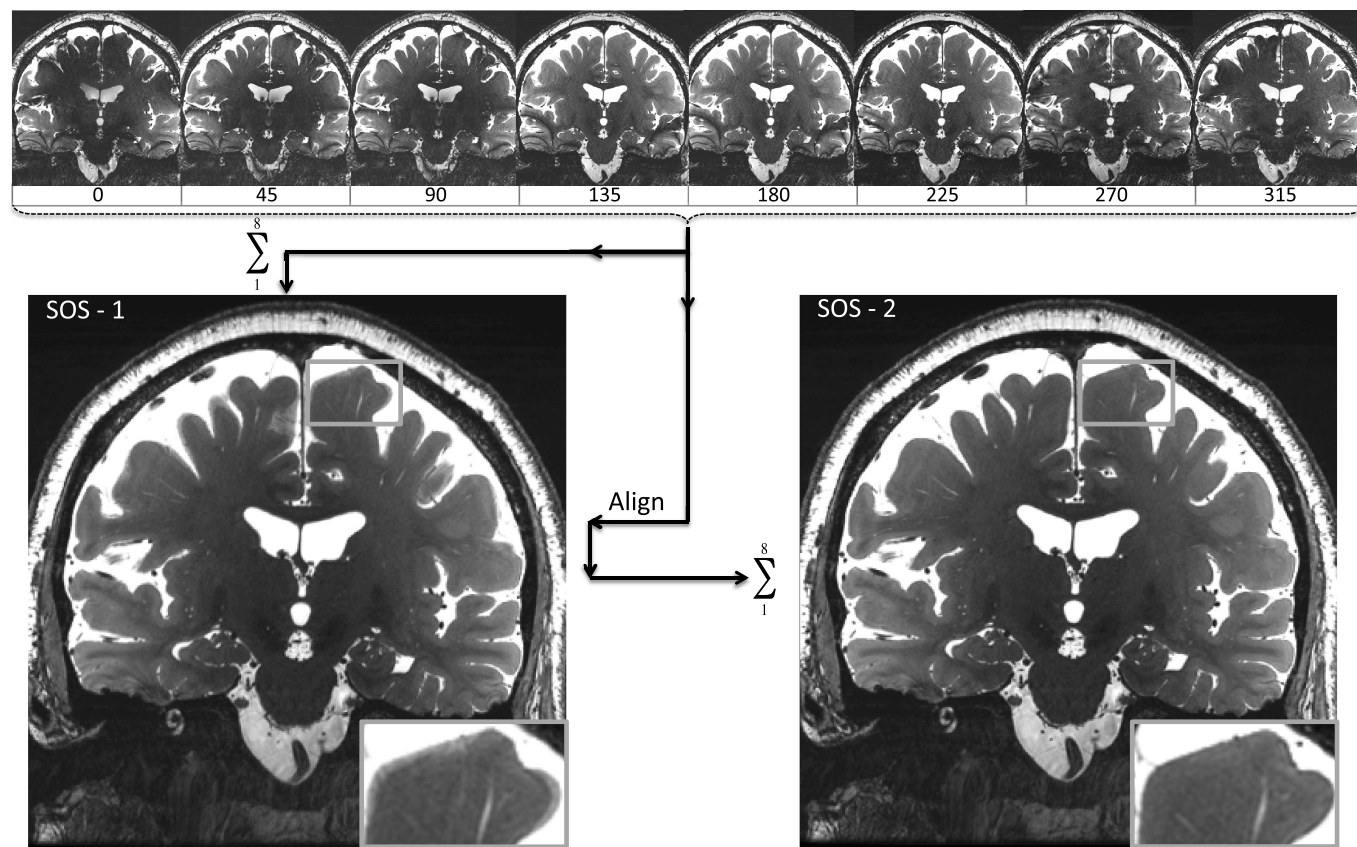


**FIGURE 1.** Averaging the 8 phase cycles from bSSFP to produce an SOS-1 image, followed by aligning the 8 phase cycles to the SOS-1 to produce a more refined SOS-2.

reconstructed to  $512 \times 512$ , 0.4-mm isotropic acquisition, 480 slices, autocalibrating reconstruction for Cartesian imaging<sup>24</sup> parallel acceleration of  $1.75 \times 1.75$ , scan time of 5 minutes 11 seconds per phase cycle). Balanced steady-state free precession demonstrates bands of hypointensity from magnetic field inhomogeneity: one can shift the location of these bands by phase cycling then average the images together to reduce or eliminate the bands.<sup>22,23</sup> Eight phase cycles were chosen to maximize the SNR and minimize banding while still being within the limits of volunteer tolerability. If an individual phase cycle was subjectively judged to be contaminated with motion, it was repeated. To compare coverage between this sequence and other sequences, 3 other imaging sequences were acquired either after the bSSFP (in the 2 patients and in 2 controls) or in a separate scanning session (the remaining 4 controls): whole-brain coronal 3D Cube T2 optimized for best gray-white contrast at 7 T (3D T2-weighted fast-spin echo with modulation of the refocusing pulses originally designed at 3 T<sup>25</sup> but optimized for 7 T, coronal, TR of 5 seconds, TE of effective 83 milliseconds, TE of actual 285 milliseconds, echo train length of 140, NEX of 1, BW of 83 kHz, autocalibrating reconstruction for Cartesian imaging of  $2 \times 2$ ,  $256 \times 256$ , FOV of 17.9 cm, 266 slices, 0.7-mm isotropic acquisition, and scan time of 9 minutes 9 seconds), 2-dimensional thin section of coronal T2-weighted FSE<sup>13</sup> (coronal oblique, TR of approximately 6 seconds, cardiac gated, TE of 47 milliseconds, refocusing FA of 140 degrees, echo train length of 8, NEX of 1, BW of 20 kHz,  $768 \times 768$ , FOV of 17 cm, slice thickness of 1.5 mm, slice gap of 0.5 mm, 16 slices,  $0.22 \times 0.22 \times 2$  mm, scan time of 10–12 minutes depending on heart rate), and 3D multiecho GRE (axial, TR of 25.6 milliseconds, 6 TEs equally spaced from 3.5–22 milliseconds using unipolar echoes, FA of 15 degrees, NEX of

1, BW of 62 kHz, array spatial sensitivity encoding technique parallel acceleration of 2,<sup>26</sup> FOV of 20 cm,  $256 \times 256$ , 186 slices, 0.8-mm isotropic, and scan time of 6 minutes 15 seconds, similar to other multiecho GRE acquisitions<sup>9</sup>). Three of the prior healthy volunteers and 1 new healthy volunteer (who also underwent bSSFP scanning but was otherwise not included in the previously mentioned analysis) were brought back for repeat scanning with 3 to 4 repetitions (3 for the 1 volunteer who underwent 6 phase cycles of bSSFP, 4 repetitions for the rest) of the 9-minute Cube T2 to provide for an additional acquisition time matched comparison to the bSSFP.

### Image Processing

Because motion can occur between bSSFP phase cycles, an alignment procedure was used (Fig. 1). Individual phase cycle images

**TABLE 1.** Rater Scoring Scale for Which bSSFP Is Compared With All Other Sequences

Score	Interpretation
1	bSSFP much worse
2	bSSFP worse
3	bSSFP mildly worse
4	bSSFP equivalent
5	bSSFP mildly better
6	bSSFP better
7	bSSFP much better

bSSFP indicates balanced steady state-free precession.

**TABLE 2.** Components of Image Analysis the Raters Scored

Hippocampal 3D multiplanar subfields for detailed segmentation
Hippocampal global evaluation for atrophy
Deep iron visualization for presurgical multiplanar planning of the 3D location of the STN
Lack of signal dropout globally (B1 homogeneity)
Conspicuity of the line of Gennari in the occipital lobe
Conspicuity of the membrane of Lilliequist
Conspicuity of cranial nerves III, V, and VI
Cortical gray-white contrast

3D indicates 3-dimensional; STN, subthalamic nucleus.

(Supplementary Digital Content 1 [single coronal slice from a single phase-cycle of bSSFP in a healthy volunteer, <http://links.lww.com/RLI/A118>] and Supplementary Digital Content 2 [coronal movie from a single phase-cycle of bSSFP in a healthy volunteer, <http://links.lww.com/RLI/A119>]) were reconstructed and combined into an initial sum-of-squares image (SOS-1). The SOS reconstruction was chosen because it has been shown to have optimal band reduction with minimal SNR loss.<sup>27</sup> The functional magnetic resonance imaging of the brain software library version 5.0 command functional magnetic resonance imaging of the brain software library Linear Registration Tool<sup>28</sup> was then used to

perform a rigid body alignment of each phase cycle to the SOS-1 using a normalized correlation cost function, interpolating with a sinc kernel and using a Hanning window of width of 7 pixels. We then recombined into a second SOS image (SOS-2), and this procedure was repeated once to produce a final reconstructed volume (SOS-3). Such iterative algorithms have been used in other image alignment procedures.<sup>29</sup> A similar alignment procedure was used for the multi-repetition Cube T2 sequences. Images for figures were captured using OsiriX (a free Digital Imaging and Communication in Medicine viewer, <http://www.osirix-viewer.com/>). Supplemental digital movies were lossy compressed with handbrake (<http://www.handbrake.fr>), which does introduce mild image smoothing.

### Image Analysis

For the assessment of iron contrast in all 8 volunteers, a 2- to 4-mm-diameter circular region of interest was placed in the center of the red nuclei on an axial section/reformat of the 3D sequences (multiecho GRE, Cube T2, and bSSFP) with a background region in the midline of the midbrain midway between the red nuclei and cerebral aqueduct. Contrast was computed as the difference divided by the sum of the mean signal in the 2 regions of interest  $\frac{|(S_{RED} - S_{BACKGROUND})|}{(S_{RED} + S_{BACKGROUND})}$ .

Images from all 8 scans were presented using an OsiriX workstation to 2 experienced neuroradiologists (authors 3 and 6), who separately compared pairs of images, specifically with bSSFP paired with Cube T2, coronal T2-weighted FSE, or multiecho GRE, rating the

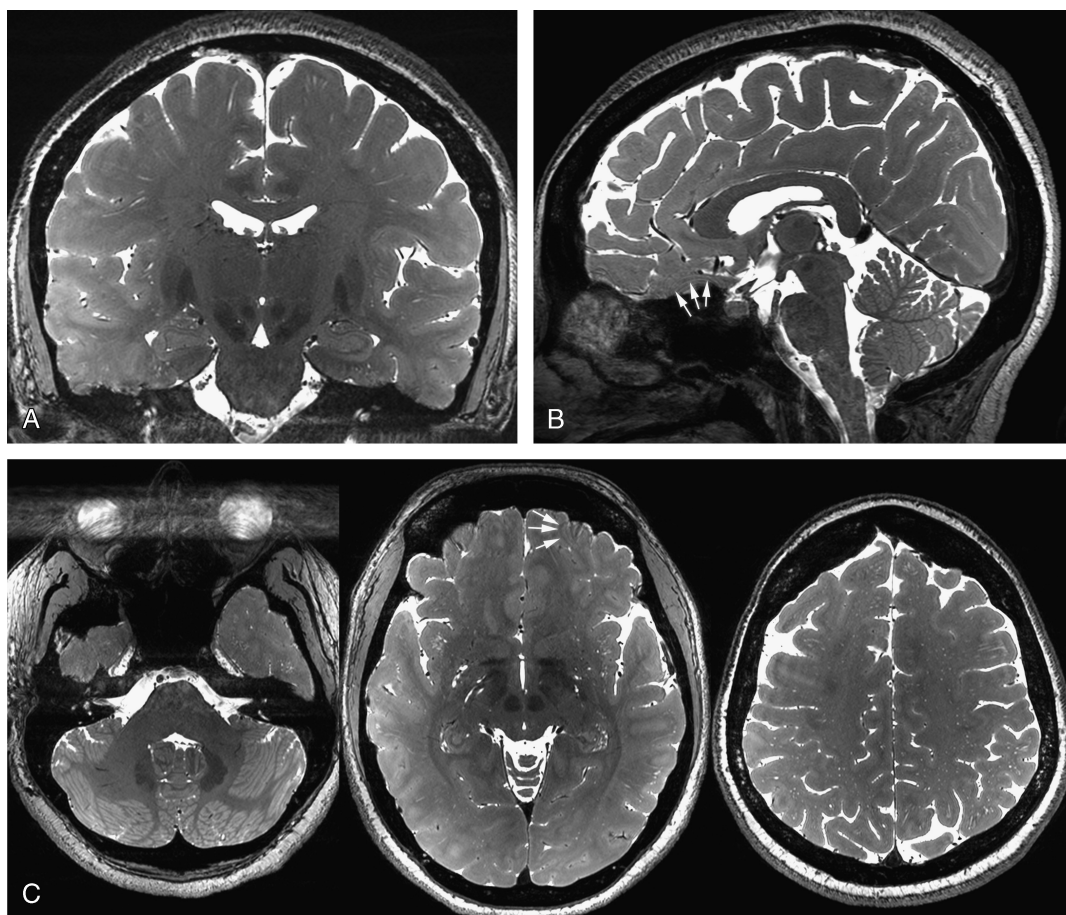


**FIGURE 2.** A to C, Coronal, sagittal, and axial views of bSSFP of 1 healthy volunteer. White arrows point to the residual banding artifact. The horizontal band of hyperintensity obscuring the orbits is artifact along the left-right phase-encode direction from ocular motion.

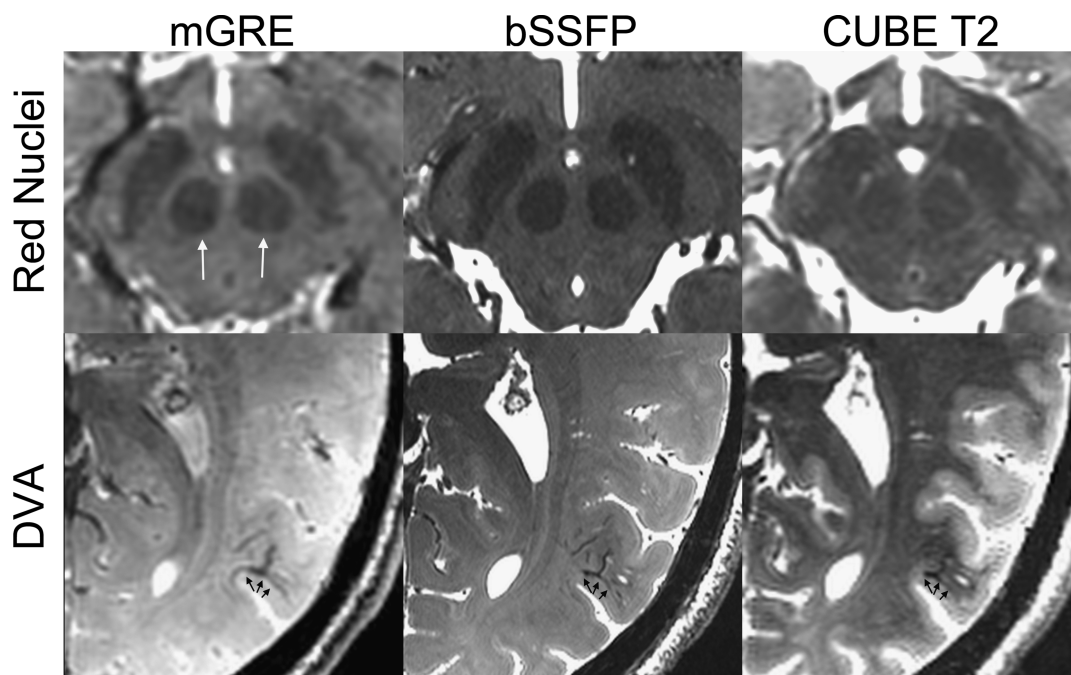


**FIGURE 3.** Comparison of iron contrast in the red nuclei (top row) and conspicuity of a developmental venous anomaly (bottom row) between multiecho GRE (left mGRE), bSSFP (middle), and Cube T2 (right) on 2 healthy volunteers.

pairs with a 7-point scale (Table 1) to provide the best range for statistical comparison on a small sample size. Each of the 8 aspects was evaluated (Table 2). Each rater was given sample images from the literature of desirable hippocampal segmentation anatomy,<sup>30</sup> subthalamic visualization,<sup>9,31–33</sup> B1 inhomogeneity,<sup>10,11</sup> and depictions of the line of Gennari and membrane of Liliequist.<sup>34,35</sup>

The overall reader agreement was assessed with linearly weighted  $\kappa$ , with confidence interval estimated by 1000 bootstrap replications. Performance of bSSFP, overall and per aspect, was evaluated by 2-sided signed-rank test against a null hypothesis of a rating of 4 (bSSFP equivalent to the other method). For the statistical tests, a Bonferroni-corrected level of 0.002 was used.

In addition, the time-matched Cube T2 was rated against the bSSFP, again using the 7-point rating scale and exclusively evaluating hippocampal 3D multiplanar subfield definition.

## RESULTS

### Examination Tolerability

The short 5-minute individual phase cycles were tolerated by the volunteers, with only 2 of the 46 phase cycles across all volunteers requiring repetition. One volunteer underwent 6 rather than 8 phase cycles because of scan time constraints and not tolerability. For 1 of the patients, 3 of the 16 phase cycles required repetition because of motion

**TABLE 3.** Rater Analysis with Median Scores Across Raters

	bSSFP Compared With		
	Multiecho GRE	Cube T2	Cor. T2-Weighted FSE
Hippocampal 3D multiplanar subfields for detailed segmentation	7*	6*	6*
Hippocampal global evaluation for atrophy	7*	4	4
Deep iron visualization for presurgical multiplanar planning of the 3D location of the STN	5	6*	4
Lack of signal dropout globally (B1 homogeneity)	5	6	7*
Conspicuity of the Line of Gennari in the occipital lobe	7*	6*	N/A
Conspicuity of the Membrane of Liliequist	5*	6*	7*
Conspicuity of cranial nerves III, V, and VI	7*	7*	7*
Cortical gray-white contrast	7*	2*	2*

\* $P < 0.002$  for the null hypothesis that bSSFP is equivalent.

1 indicates bSSFP much worse; 7, bSSFP much better; 3D, 3-dimensional; bSSFP, balanced steady state-free precession; Cor., Coronal; FSE, fast spin echo; GRE, gradient recalled echo; N/A, the field of view of the coronal T2-weighted FSE did not include the calcarine sulcus; STN, subthalamic nucleus.

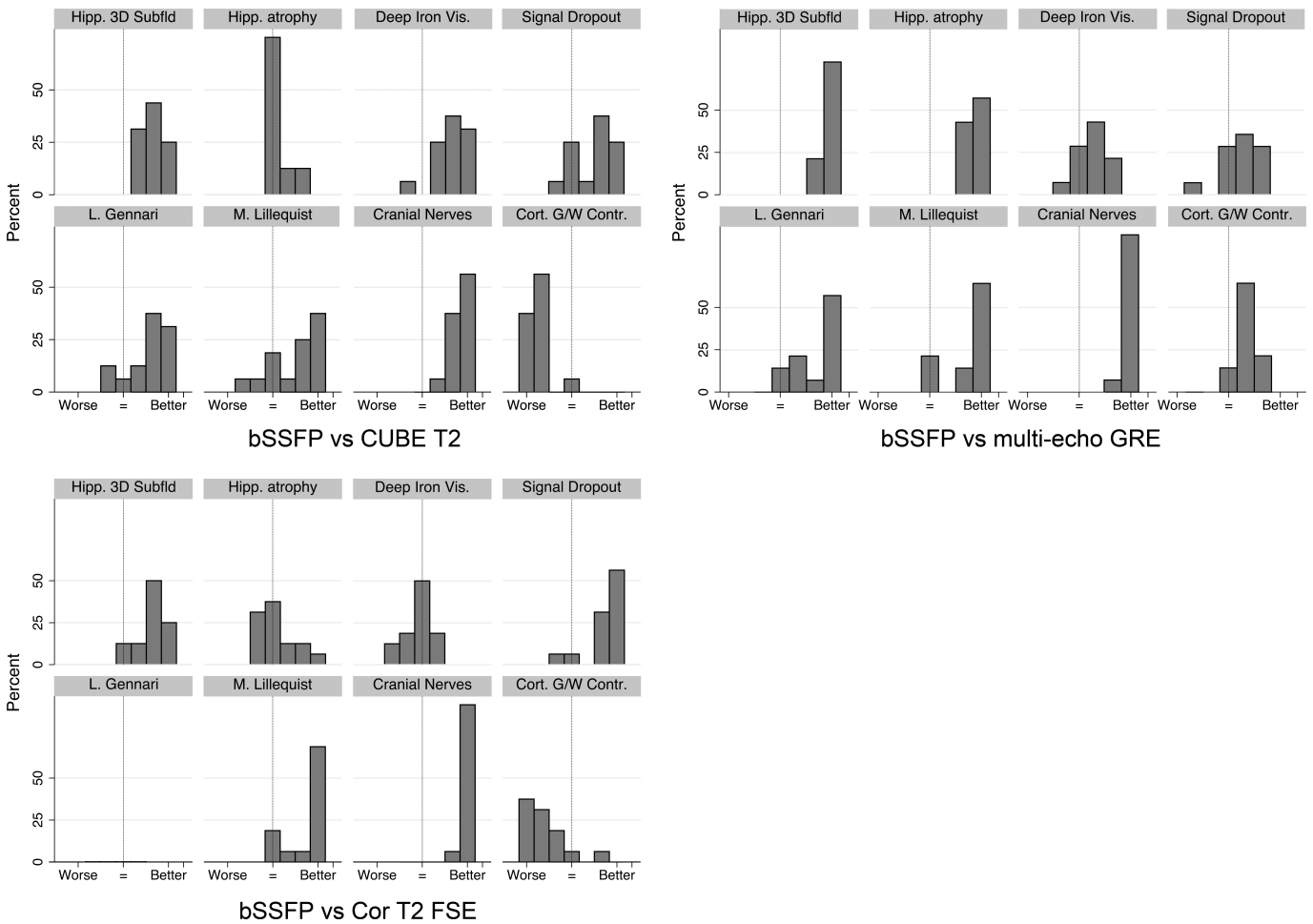


**FIGURE 4.** Histograms of rater scores for bSSFP versus multiecho GRE/corresponding T2-weighted FSE/Cube T2.

artifact; for this reason, this volunteer did not undergo multiecho GRE imaging. The other patient did not require repetition. Although not specifically asked, the raters commented on motion artifact in coronal T2-weighted FSE (2 cases for 1 rater, 1 case for the other rater), Cube T2 (1 and 1), and multiecho GRE (2 and 0), but not for bSSFP.

**General Imaging Findings**

The bSSFP images showed very little motion artifact and were relatively uniform in signal intensity across the intracranial structures, with an unusually high homogeneity considering these are uncorrected 7 T images (Fig. 2, Supplementary Digital Content 3 [coronal movie from an eight-phase-cycle bSSFP in a healthy volunteer, <http://links.lww.com/RLI/A120>], Supplementary Digital Content 4 [axial movie from an eight-phase-cycle bSSFP in a healthy volunteer, <http://links.lww.com/RLI/A121>], Supplementary Digital Content 5 [sagittal movie from an eight-phase-cycle bSSFP in a healthy volunteer, <http://links.lww.com/RLI/A122>]). Banding is much reduced compared with a single phase cycle (Supplementary Digital Content 1 [<http://links.lww.com/RLI/A118>] and Supplementary Digital Content 2 [<http://links.lww.com/RLI/A119>]) but still visible near the bases of the frontal and temporal lobes (white arrows on Figs. 2B and C). Normal perivascular spaces are highly conspicuous (Fig. 2C).

**Iron Contrast**

Iron contrast in the red nuclei measured similarly between bSSFP ( $0.200 \pm 0.030$ ), Cube T2 ( $0.189 \pm 0.158$ , paired *t* test;  $P > 0.05$ ), and

coronal T2-weighted FSE ( $0.182 \pm 0.022$ ;  $P > 0.05$ ), but bSSFP had a slightly better contrast than that of multiecho GRE ( $0.144 \pm 0.043$ ;  $P = 0.002$ ) (Fig. 3, top row). Venous contrast was well demonstrated in a normal-variant developmental venous anomaly (DVA; Fig. 3, bottom row).

**Rater Analysis of 7 T bSSFP With Multiecho GRE, Cube T2, and Thin-Section Coronal T2-Weighted FSE**

Balanced steady state-free precession compared with multiecho GRE, Cube T2, and coronal T2-weighted FSE demonstrated  $\kappa$  of 0.36, 0.67, and 0.60, respectively. The low  $\kappa$  values are likely caused by the small sample size and small number of reviewers; observed agreement was very high (84%–90%) (Table 3; Fig. 4).

**Hippocampus**

The global clinical evaluation of hippocampal atrophy was similar to both Cube and coronal T2-weighted FSE (Fig. 5). The hippocampus demonstrated intricate detail in all 3 planes with bSSFP, however, and this provided a superior 3-dimensional depiction of hippocampal morphology that would be suitable to segmentation studies (Fig. 6, rater analysis,  $P < 0.0005$ ). For example, the hypointense band within the hippocampus (termed the *stratum radiatum* and *lacunosum-moleculare* of field cornu ammonis 1, although also containing white-matter fibers) is well seen in the coronal plane on the 3 sequences (Fig. 5), but the bSSFP surpasses all of them because it has the highest isotropic

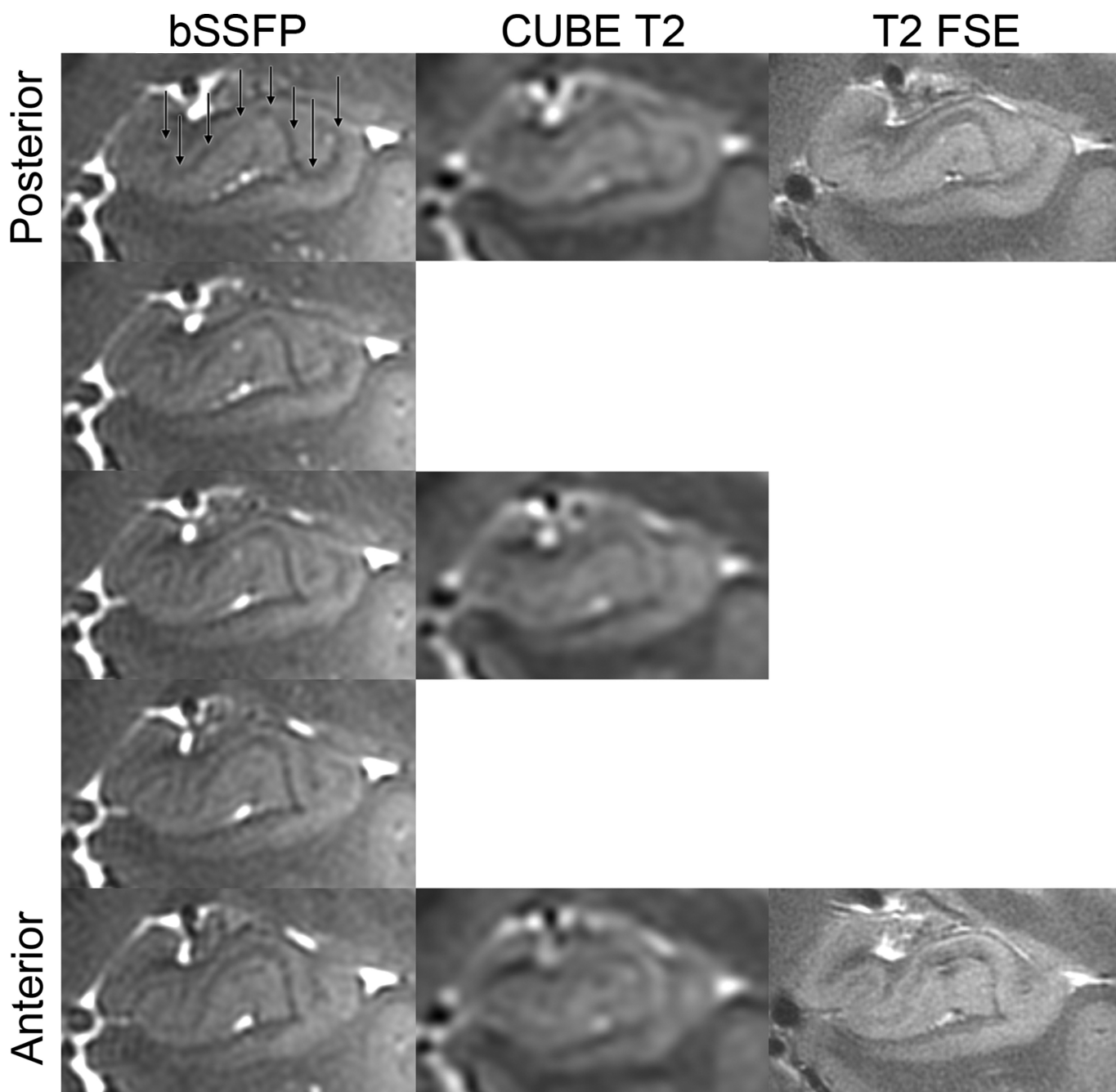


**FIGURE 5.** Comparison of left hippocampal head anatomy on bSSFP, matched posterior-to-anterior sections in a healthy volunteer. Black arrows point to the layer stratum radiatum and lacunosum-moleculare,<sup>30,46–48</sup> the hypointense band centrally within the hippocampus. Images for the Cube T2 and T2-weighted FSE are displayed in native space without alignment or interpolation.

resolution and enough contrast to fully delineate the 3D microstructure in all 3 planes (Fig. 6). The bSSFP was still rated as superior to the time-matched Cube T2 for segmentation purposes in 3 of 4 healthy volunteers by both raters (Fig. 7). In 1 healthy volunteer, the bSSFP was slightly better than the Cube T2 for 1 rater and vice versa for the other rater.

#### Visualization of the Subthalamic Nucleus

Deep gray structures such as the subthalamic nucleus were readily apparent and visually separable from the adjacent substantia

nigra in both the coronal and sagittal planes (Fig. 8). Coronal T2-weighted FSE achieved an equivalent contrast as judged by the raters but is impractical for presurgical planning and for volumetry/segmentation because of its anisotropic voxel size. Balanced steady state-free precession was deemed superior to Cube T2, likely because of the higher resolution. Balanced steady state-free precession offered a slightly better visualization than did multiecho GRE ( $P = 0.01$ , not significant after Bonferroni correction) and achieved a notably higher spatial resolution than did multiecho GRE.

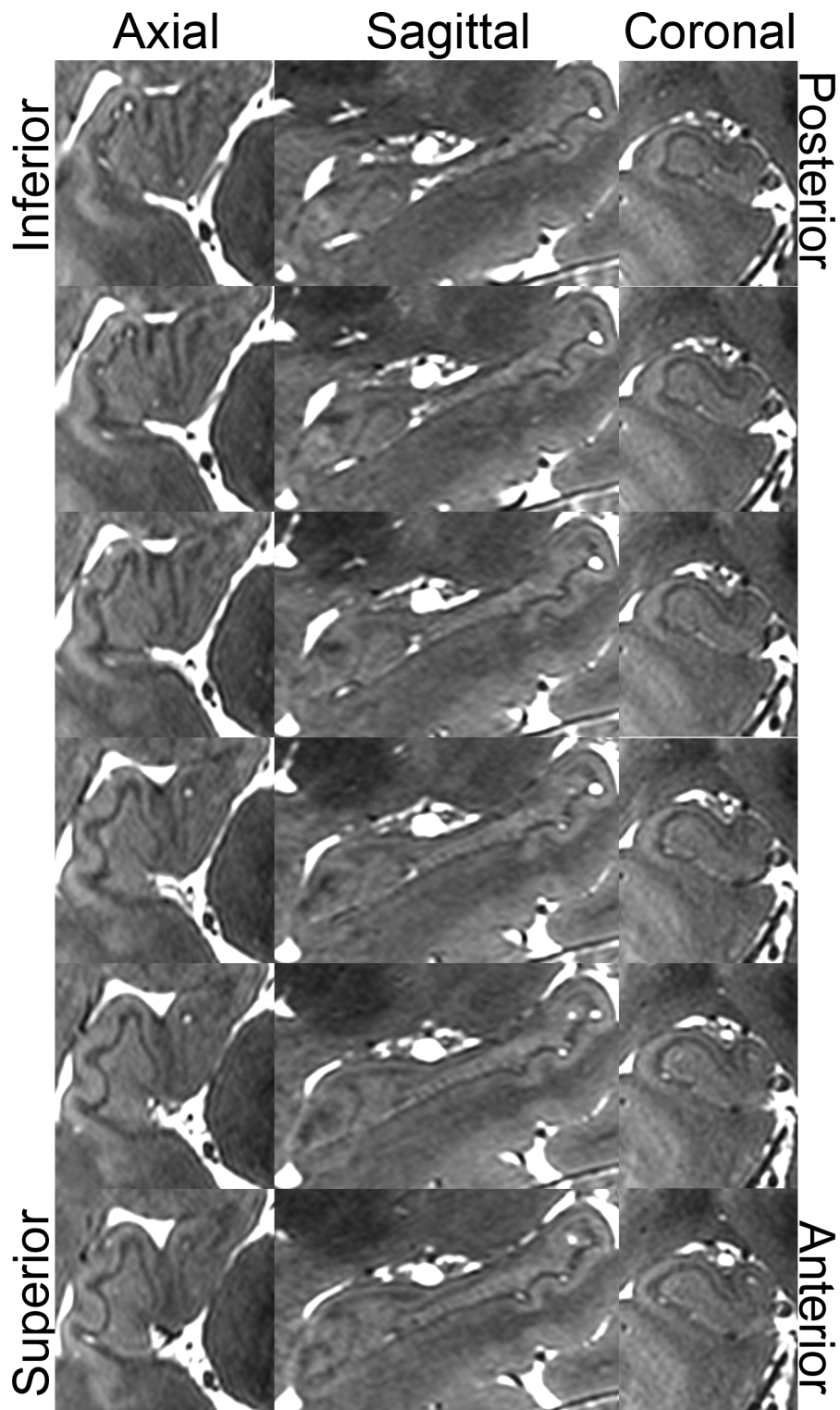


**FIGURE 6.** Right hippocampal head anatomy in a healthy volunteer as visualized by bSSFP. Sagittal progresses from medial (top) to lateral (bottom).

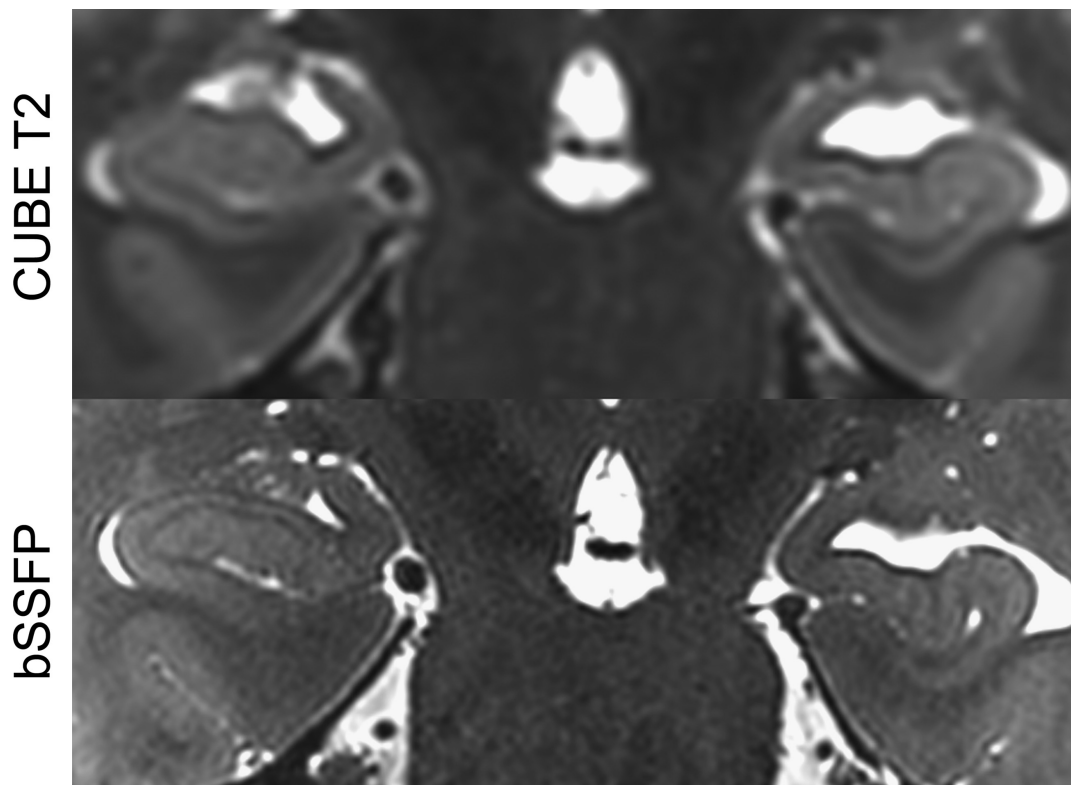


**FIGURE 7.** Hippocampal heads in a healthy volunteer in time-matched Cube T2 (top) and bSSFP (bottom). The left-right asymmetry is caused by a slight head rotation.

### B1 Homogeneity

Homogeneity of bSSFP was superior across the intracranial structures compared with the 2-dimensional FSE ( $P = 0.0005$ ) and demonstrated a slightly better homogeneity compared with Cube and multiecho GRE ( $P = 0.0025$  and  $0.02$ , respectively, not significant after the Bonferroni correction) without any image correction (Fig. 9). Although most 7 T studies suffer from poor visibility of the posterior fossa, bSSFP demonstrated intricate details of the cerebellum (Fig. 2).

### Microscopic Anatomy

On all of the other features of intricate microstructure tested, bSSFP performance was equal to or better than that of the other sequences (Table 3). The balance of high resolution and iron sensitivity in bSSFP facilitates superior visualization of the line of Gennari.<sup>34</sup> It was best seen in the coronal plane in the bSSFP sequence and clearly identified in 6 of the 8 volunteers for each rater (Fig. 10). This was difficult to visualize in all other sequences. In addition, the membrane of Liliequist was well seen in 6 of the 8 volunteers (Fig. 11), significantly better than multiecho GRE and coronal T2-weighted FSE and slightly better than the Cube T2 ( $P = 0.0012$ ,  $P = 0.0004$ , and  $P = 0.0059$ , uncorrected, respectively). Balanced steady state-free precession provided superior visualization of the adjacent third, fifth, and sixth cranial nerves, and CSF was identified, tracking along the abducens nerve as it traversed the skull base (Fig. 12).

### Cortical Gray-White Contrast

Gray-white contrast with bSSFP was significantly better compared with multiecho GRE but significantly lacking compared with the coronal T2-weighted FSE and Cube T2 (Figs. 3 and 9).

### DISCUSSION

Balanced steady state-free precession has typically been used clinically for the evaluation of extra-axial structures such as cisternal segments of cranial nerves, and this study demonstrates that this advantage over other sequences remains true at 7 T. Moreover, we have demonstrated the utility of bSSFP in other regions of the brain. Because of bSSFP's intrinsically high SNR, we can collect a single 0.5-NEX imaging volume in 5 minutes at 0.4-mm isotropic resolution. This offers both (1) imaging time per sequence that is tolerable for most subjects and (2) an image SNR adequate for alignment (Supplementary Digital Content 1 [<http://links.lww.com/RLI/A118>] and Supplementary Digital Content 2 [<http://links.lww.com/RLI/A119>]). Several phase cycles allows us to further improve SNR and reduce banding using a simple alignment and averaging procedure. Because typical clinical scanning can require sometimes 10 or more 5-minute sequences, this paradigm does not fall out of the range of patient tolerance, although there may be a limited time for other sequences within a scanning session.

To our knowledge, no other work in the field has explored 7 T bSSFP for high-resolution brain imaging. We have demonstrated that this sequence allows superior depiction of the medial temporal lobe and cortical microstructure such as the line of Gennari, and it rivals typical iron-sensitive multiecho GRE for deep brain iron-containing nuclei. Extensive prior efforts at high-field imaging have shown the line of Gennari, but most of these were not isotropic whole-brain imaging protocols that yielded contrast useful for multiple brain regions.<sup>21,36</sup> The benefit of bSSFP likely stems from the coupling of ultrahigh resolution with iron sensitivity. Of note, manipulation of the echo-train length and alteration of the modulation of flip angles could increase the iron contrast for Cube T2, albeit at the cost of blurring and reduced

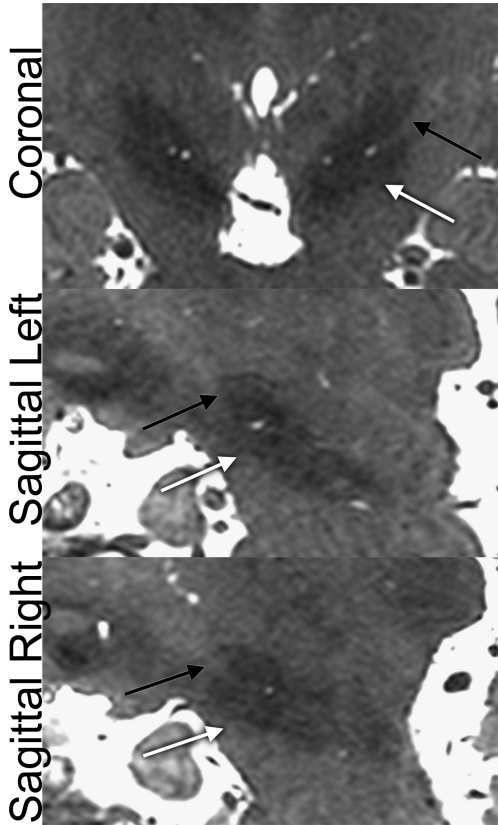


**FIGURE 8.** Subthalamic nucleus localization in a healthy volunteer as visualized by bSSFP. Black arrow indicates STN; white arrow, substantia nigra.

SNR. Whereas high-resolution imaging of the human hippocampus has generally been achieved with anisotropic imaging,<sup>37–40</sup> a recent study used isotropic imaging with a 0.6-mm voxel size at 3.0 T, although this study used six 16-minute individual acquisitions that would be difficult to translate clinically.<sup>41</sup> In contrast, our work confirms clinical feasibility with the inclusion of 2 patients in this study. The 0.4-mm isotropic resolution surpasses all that has been performed to date in the literature. At our high resolution, the hippocampus shows impressive contrast because less partial volume averaging is occurring. This resolution and definition of the subthalamic nucleus could facilitate better intraoperative planning and be complementary to techniques that offer high contrast in the upper brainstem.<sup>42,43</sup> If higher flip angle acquisitions were to be attempted, the SAR could be mitigated by pauses or other low-SAR sequences intermingled between phase cycles. This advance demonstrates that ultrahigh-field imaging can provide novel benefits for the fields of neuroscience and neuroradiology.

Limitations of bSSFP are that contrast near the cortex is limited and that gray-white distinction is poor. Future efforts could include white matter or CSF nulling to provide improved contrast, although this will be at the cost of SNR and, secondarily, image resolution. Pulsatility artifact does occur, particularly along the phase-encode direction (right-left) at the level of the circle of Willis, and this can obscure the base of the temporal lobe and hippocampal head. Although cardiac gating is challenging at this short TR, CSF and/or blood nulling may remedy this artifact. Further TR shortening to reduce pulsatility at this resolution would be impossible, given that we are already at maximum possible BW and minimum TR and TE. Similarly, reducing the flip angle would decrease the T2 contrast and increase the T2\* contrast, altering the image contrast. The image registration algorithm worked well for the 6 volunteers and the 2 patients, likely because the brain-CSF interface drove the registration, overcoming the obstacle of banding artifact. The need to repeat sequences obscured by motion artifact could prove limiting under some circumstances, but, generally, patients can refrain from moving for 5 minutes at a time for at least 30 minutes. Access to 7 T scanners is still limited with approximately 50 to 60 worldwide. The rating portion of this study had a low  $\kappa$  for the comparison of bSSFP

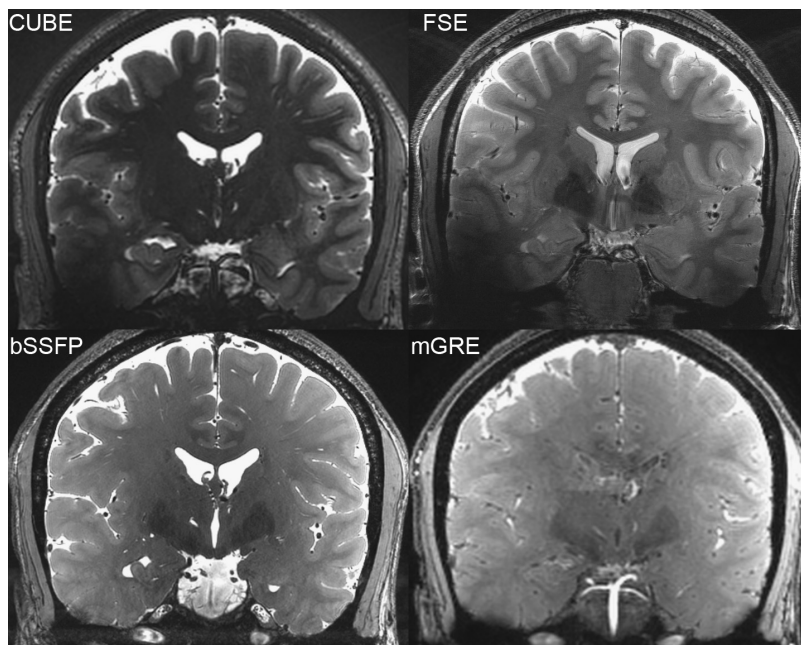


**FIGURE 9.** Relative homogeneity of B1 in bSSFP in a healthy volunteer. However, cortical gray-white contrast is still better in Cube T2 and T2-weighted FSE.

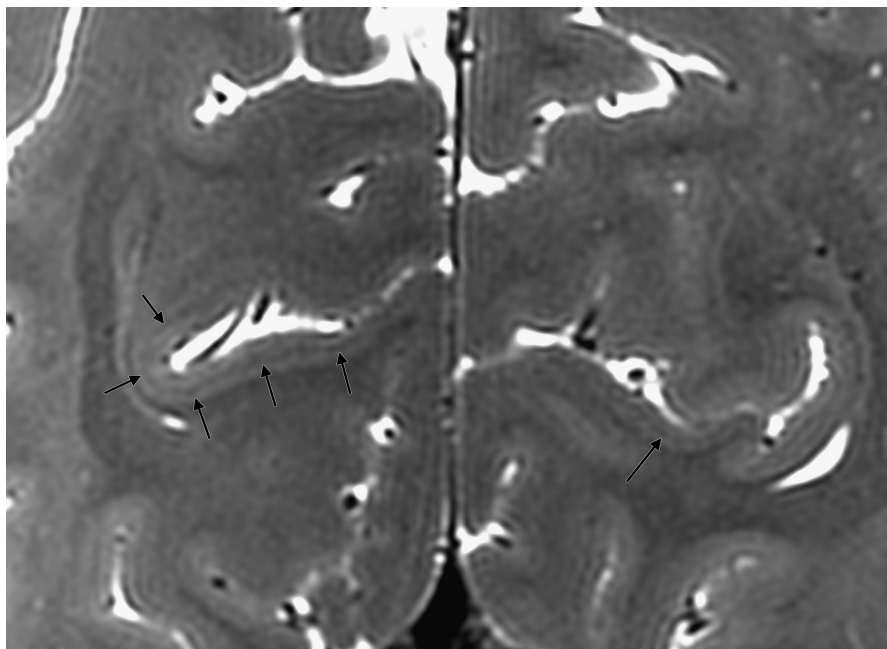


FIGURE 10. Conspicuity of the line of Gennari on coronal bSSFP in a healthy volunteer.

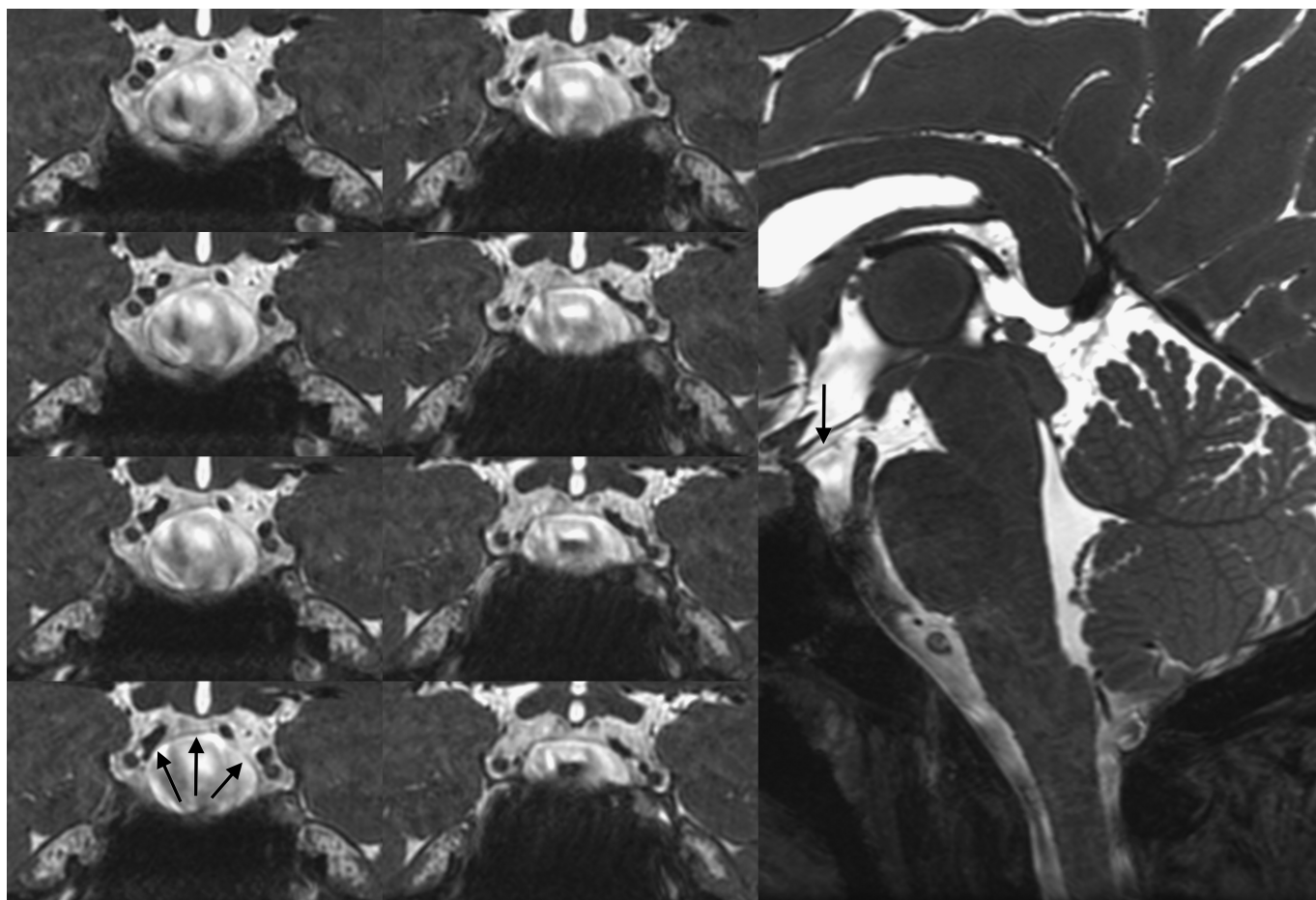


FIGURE 11. Conspicuity of the membrane of Lilliequist on coronal and sagittal bSSFP in a healthy volunteer.

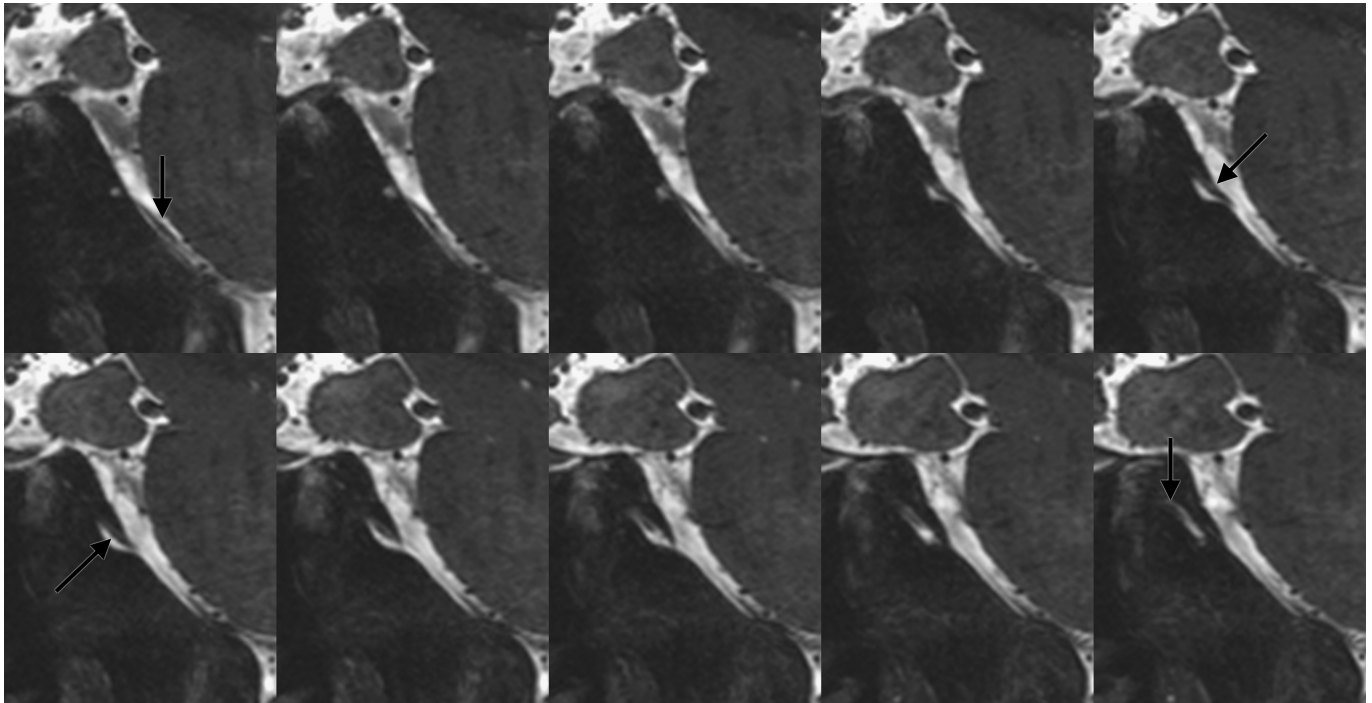


FIGURE 12. Abducens nerve on sagittal bSSFP in a healthy volunteer.

with multiecho GRE; nevertheless, the ratings clearly show that bSSFP has superior contrast for the hippocampi, skull base, and neocortical gray-white differentiation, although both have equivalent iron sensitivity and B1 homogeneity. Another limitation of the global ratings portion of this study is that scan times were not equivalent in the global comparison, with bSSFP having 4-times-longer scanning than T2-weighted FSE or Cube T2, effectively doubling the expected SNR of the bSSFP in comparison. Nevertheless, the comparison of time-matched bSSFP with Cube T2 still showed superiority of the bSSFP for 3-dimensional hippocampal subfield delineation, likely secondary to the high SNR coupled with the high resolution. Part of the strength of bSSFP is that 1 complete high-resolution volume with adequate SNR for alignment can be acquired in only 5 minutes. Even if 1 or even 2 phase cycles are corrupted by motion, that constitutes a small portion of the overall data that could be ignored or quickly repeated as done in this study. Such short scan times could prove more challenging for the other sequences: the coronal T2-weighted FSE is anisotropic, so aligning repetitions is more difficult; the Cube T2 and multiecho GRE require more time to encode all of k-space, and single-echo GRE will have a lower intrinsic SNR because signal is not fully refocused at the end of each TR period. Whereas single-echo or multiecho GRE can provide superior iron sensitivity through susceptibility processing,<sup>44,45</sup> the resolution in this study surpasses current in vivo efforts at susceptibility mapping. Finally, this study did examine a small number of volunteers using only 2 raters, so future studies and clinical experience will be needed to reinforce the clinical utility of bSSFP.

Our future work will take advantage of this extremely high-resolution imaging of the medial temporal lobe to segment the microstructure of the hippocampus. This improved high-resolution sequence could also be applied to imaging of the healthy brain as well as disease states such as the Alzheimer disease and epilepsy. In addition, the detailed depictions of deep-brain iron containing nuclei could be beneficial for both surgical targeting and quantitative studies of microstructure associated with Parkinson disease and other movement disorders.

## REFERENCES

1. Ugurbil K. The road to functional imaging and ultrahigh fields. *Neuroimage*. 2012;62:726–735.
2. van der Kolk AG, Hendrikse J, Zwanenburg JJ, et al. Clinical applications of 7 T MRI in the brain. *Eur J Radiol*. 2013;82:708–718.
3. Abduljalil AM, Kangarlu A, Zhang X, et al. Acquisition of human multislice MR images at 8 Tesla. *J Comput Assist Tomogr*. 1999;23:335–340.
4. Bourekas EC, Christoforidis GA, Abduljalil AM, et al. High resolution MRI of the deep gray nuclei at 8 Tesla. *J Comput Assist Tomogr*. 1999;23:867–874.
5. Burgess RE, Yu Y, Abduljalil AM, et al. High signal-to-noise FLASH imaging at 8 Tesla. *Magn Reson Imaging*. 1999;17:1099–1103.
6. Robitaille PM, Abduljalil AM, Kangarlu A. Ultra high resolution imaging of the human head at 8 tesla: 2K x 2K for Y2K. *J Comput Assist Tomogr*. 2000; 24:2–8.
7. Christoforidis GA, Bourekas EC, Baujan M, et al. High resolution MRI of the deep brain vascular anatomy at 8 tesla: susceptibility-based enhancement of the venous structures. *J Comput Assist Tomogr*. 1999;23:857–866.
8. Li TQ, van Gelderen P, Merkle H, et al. Extensive heterogeneity in white matter intensity in high-resolution T2\*-weighted MRI of the human brain at 7.0 T. *Neuroimage*. 2006;32:1032–1040.
9. Deistung A, Schafer A, Schweser F, et al. Toward in vivo histology: a comparison of quantitative susceptibility mapping (QSM) with magnitude-, phase-, and R2\*-imaging at ultra-high magnetic field strength. *Neuroimage*. 2013;65: 299–314.
10. Lusebrink F, Wollrab A, Speck O. Cortical thickness determination of the human brain using high resolution 3T and 7T MRI data. *Neuroimage*. 2013;70:122–131.
11. Marques JP, Kober T, Krueger G, et al. MP2RAGE, a self bias-field corrected sequence for improved segmentation and T1-mapping at high field. *Neuroimage*. 2010;49:1271–1281.
12. Visser F, Zwanenburg JJ, Hoogduin JM, et al. High-resolution magnetization-prepared 3D-FLAIR imaging at 7.0 Tesla. *Magn Reson Med*. 2010;64:194–202.
13. Kerchner GA, Deutsch GK, Zeineh M, et al. Hippocampal CA1 apical neuropil atrophy and memory performance in Alzheimer's disease. *Neuroimage*. 2012;63: 194–202.
14. Hoult DI, Phil D. Sensitivity and power deposition in a high-field imaging experiment. *J Magn Reson Imaging*. 2000;12:46–67.
15. Ibrahim TS, Lee R, Baertlein BA, et al. Effect of RF coil excitation on field inhomogeneity at ultra high fields: a field optimized TEM resonator. *Magn Reson Imaging*. 2001;19:1339–1347.
16. Katscher U, Bornert P, Leussler C, et al. Transmit SENSE. *Magn Reson Med*. 2003;49:144–150.
17. Zhu Y. Parallel excitation with an array of transmit coils. *Magn Reson Med*. 2004;51:775–784.

18. Sheth S, Branstetter BF, Escott EJ. Appearance of normal cranial nerves on steady-state free precession MR images. *Radiographics*. 2009;29:1045–1055.
19. Ronald JA, Chen Y, Bernas L, et al. Clinical field-strength MRI of amyloid plaques induced by low-level cholesterol feeding in rabbits. *Brain*. 2009; 132(pt 5):1346–1354.
20. Scheffler K, Lehnardt S. Principles and applications of balanced SSFP techniques. *Eur Radiol*. 2003;13:2409–2418.
21. Lee J, Fukunaga M, Duyn JH. Improving contrast to noise ratio of resonance frequency contrast images (phase images) using balanced steady-state free precession. *Neuroimage*. 2011;54:2779–2788.
22. Bieri O, Scheffler K. On the origin of apparent low tissue signals in balanced SSFP. *Magn Reson Med*. 2006;56:1067–1074.
23. Elliott AM, Bernstein MA, Ward HA, et al. Nonlinear averaging reconstruction method for phase-cycle SSFP. *Magn Reson Imaging*. 2007;25:359–364.
24. Brau AC, Beatty PJ, Skare S, et al. Comparison of reconstruction accuracy and efficiency among autocalibrating data-driven parallel imaging methods. *Magn Reson Med*. 2008;59:382–395.
25. Busse RF. Reduced RF power without blurring: correcting for modulation of refocusing flip angle in FSE sequences. *Magn Reson Med*. 2004;51:1031–1037.
26. Pruessmann KP, Weiger M, Scheidegger MB, et al. SENSE: sensitivity encoding for fast MRI. *Magn Reson Med*. 1999;42:952–962.
27. Bangerter NK, Hargreaves BA, Vasanaawala SS, et al. Analysis of multiple-acquisition SSFP. *Magn Reson Med*. 2004;51:1038–1047.
28. Jenkinson M, Bannister P, Brady M, et al. Improved optimization for the robust and accurate linear registration and motion correction of brain images. *Neuroimage*. 2002;17:825–841.
29. Zeineh MM, Holdsworth S, Skare S, et al. Ultra-high resolution diffusion tensor imaging of the microscopic pathways of the medial temporal lobe. *Neuroimage*. 2012;62:2065–2082.
30. Yushkevich PA, Avants BB, Pluta J, et al. A high-resolution computational atlas of the human hippocampus from postmortem magnetic resonance imaging at 9.4 T. *Neuroimage*. 2009;44:385–398.
31. Lenglet C, Abosch A, Yacoub E, et al. Comprehensive in vivo mapping of the human basal ganglia and thalamic connectome in individuals using 7T MRI. *PLoS ONE*. 2012;7:e29153.
32. Naidich TP, Duvernoy HM, Delman BN, et al. *Duvernoy's Atlas of the Human Brain Stem and Cerebellum: High-Field MRI: Surface Anatomy, Internal Structure, Vascularization and 3D Sectional Anatomy*. Wien, NY: Springer; 2009:398–399.
33. Fatterpekar GM, Delman BN, Boonn WW, et al. MR microscopy of normal human brain. *Magn Reson Imaging Clin N Am*. 2003;11:641–653.
34. Fukunaga M, Li TQ, van Gelderen P, et al. Layer-specific variation of iron content in cerebral cortex as a source of MRI contrast. *Proc Natl Acad Sci U S A*. 2010;107:3834–3839.
35. Fushimi Y, Miki Y, Ueba T, et al. Lilliequist membrane: three-dimensional constructive interference in steady state MR imaging. *Radiology*. 2003;229: 360–365.
36. Duyn JH, van Gelderen P, Li TQ, et al. High-field MRI of brain cortical substructure based on signal phase. *Proc Natl Acad Sci U S A*. 2007;104:11796–11801.
37. Kerchner GA. Ultra-high field 7T MRI: a new tool for studying Alzheimer's disease. *J Alzheimers Dis*. 2011;26(suppl 3):91–95.
38. Mueller SG, Chao LL, Berman B, et al. Evidence for functional specialization of hippocampal subfields detected by MR subfield volumetry on high resolution images at 4 T. *Neuroimage*. 2011;56:851–857.
39. Burggren AC, Zeineh MM, Ekstrom AD, et al. Reduced cortical thickness in hippocampal subregions among cognitively normal apolipoprotein E e4 carriers. *Neuroimage*. 2008;41:1177–1183.
40. Zeineh MM, Engel SA, Thompson PM, et al. Dynamics of the hippocampus during encoding and retrieval of face-name pairs. *Science*. 2003;299:577–580.
41. Winterburn JL, Pruessner JC, Chavez S, et al. A novel in vivo atlas of human hippocampal subfields using high-resolution 3 T magnetic resonance imaging. *Neuroimage*. 2013;74:254–265.
42. Sudhyadhom A, Haq IU, Foote KD, et al. A high resolution and high contrast MRI for differentiation of subcortical structures for DBS targeting: the fast gray matter acquisition T1 inversion recovery (FGATIR). *Neuroimage*. 2009; 47(suppl 2):T44–T52.
43. Tourdias T, Saranathan M, Levesque IR, et al. Visualization of intrathalamic nuclei with optimized white-matter-nulled MPRAGE at 7T. *Neuroimage*. 2014;84:534–545.
44. Liu T, Liu J, de Rochefort L, et al. Morphology enabled dipole inversion (MEDI) from a single-angle acquisition: comparison with COSMOS in human brain imaging. *Magn Reson Med*. 2011;66:777–783.
45. Schafer A, Forstmann BU, Neumann J, et al. Direct visualization of the subthalamic nucleus and its iron distribution using high-resolution susceptibility mapping. *Hum Brain Mapp*. 2012;33:2831–2842.
46. Kerchner GA, Hess CP, Hammond-Rosenbluth KE, et al. Hippocampal CA1 apical neuropil atrophy in mild Alzheimer disease visualized with 7-T MRI. *Neurology*. 2010;75:1381–1387.
47. Insausti R, Amaral DG. Hippocampal formation. In: Paxinos G, Mai JK, eds. *The Human Nervous System*. 2nd ed. Amsterdam: Elsevier; 2004:871–914.
48. Duvernoy HM. *The Human Hippocampus: Functional Anatomy, Vascularization and Serial Sections with MRI*. 3rd ed. Heidelberg, Berlin: Springer-Verlag; 2005:129–163.